# Fracture of a ductile layer constrained by stiff substrates

S.-H. CHOI[1], B.-G. SONG[1], K.-J. KANG[1] and N. A. FLECK[2]

[1]*Department of Mechanical Engineering, Chonnam National University, Kwangju, Republic of Korea and* [2]*Cambridge University Engineering Department, Trumpington Street, Cambridge, UK*

*Received in final form 17 October 2000*

**ABSTRACT** A combined experimental and theoretical analysis of the fracture behaviour of brass/solder/brass sandwich specimens is conducted. First, the theories of interfacial fracture initiation for a ductile layer sandwiched between elastic substrates are reviewed. The fracture behaviours are then reported of brass/solder/brass sandwich specimens under various mode mixities. Additionally, the effects of solder layer thickness $h$ and specimen lateral thickness $t$ are presented. The effects of mode mix and plastic constraint on the failure mechanism and toughness are analysed.

**Keywords** ductile fracture; interface fracture; mixed-mode loading; sandwich specimen; solder joint

## INTRODUCTION

Many mechanical and electrical engineering components are made by combining two or more materials. Ceramic/metal composites, cutting tool/bits, and surface-mounted electronic packages are typical examples in which stiff substrates are bonded to ductile layers. An analysis of the potential failure modes of bimaterials is essential to ensure the reliability of such components.

The interfacial fracture of dissimilar materials has been widely studied, see for example recent comprehensive reivew by Hutchinson and Suo.[1] Although theories of elastic–brittle interfacial fracture have been established using linear elastic fracture mechanics (LEFM), many elastic–plastic fracture problems remain. Shih and Asaro[2] have shown that the stress field near an interface crack is similar to the Hutchinson–Rice–Rosengren (HRR) field near a crack tip with a homogeneous material under mixed mode loading. The interfacial field can be characterized by two parameters: the $J$-integral and the mode mix.

In the experimental studies of Evans and his colleagues,[3–5] O'Dowd *et al.*[6] and Thurston and Zehnder[7] the plastic zone within the sandwiched metal layer is much smaller than the layer thickness, and so the degree of plastic constraint imposed by the substrates is negligible. Evans and co-workers[3–5] measured the interfacial fracture toughness of various ceramic/metal/ceramic sandwiches in terms of the elastic energy release rate $G$, since the degree of plastic deformation in the sandwiched metallic layer was negligible. O'Dowd *et al.*[6] measured the fracture toughness of alumina–niobium interfaces and used the interfacial stress intensity factor $K$ as the fracture parameter. Depending upon the mode mix, the fracture was either interfacial or was within the alumina substrate. Thurston and Zehnder[7] used the $J$-integral to characterize the interfacial toughness of silica/copper/silica.

Varias *et al.*[8] analysed the case where the interfacial bonding strength between a ductile layer and stiff, tough substrates is sufficiently high to allow the layer to undergo substantial plastic deformation; they found that the maximum stress develops at several layer thicknesses ahead of the crack tip. In this case fracture may occur by void growth or by brittle debonding a finite distance ahead of the crack tip, and it is considerably affected by plastic deformation within the ductile layer. The failures of many bonded joints, such as the soldered joints of electronic packages or the brazed joints of machine tools, are accompanied by substantial plastic deformation. However, as mentioned above, few studies of this class of failure exist in the literature.

In this article we shall review the theories of interfacial fracture initiation for a ductile layer sandwiched between elastic substrates. The fracture behaviours are then reported for mixed mode loading of brass/solder/brass sandwich specimens. Additionally, the effects of solder

*Correspondence:* Professor Ki-Ju Kang, Department of Mechanical Engineering, Chonnam National University, Kwangju 500-757, Republic of Korea.
E-mail: kjkang@chonnam.ac.kr

layer thickness $h$ and specimen lateral thickness $t$ are presented. The effects of mode mix and plastic constraint on the failure mechanism and toughness are both measured and analysed.

## FRACTURE MECHANISMS

Interfacial fracture in a ductile layer constrained by stiff substrates is triggered by one of four mechanisms as illustrated in Fig. 1, and as discussed by O'Dowd *et al.*[6] and Varias *et al.*[8] The first mechanism is near-tip void growth and coalescence, as shown in Fig. 1(a) and hereafter called fracture mechanism 1. It is commonly observed in the ductile fracture of homogeneous materials. Assuming that the crack begins to advance when the crack tip is opening is of the order of the mean spacing between pre-existing voids in front of the crack tip, the fracture toughness can be written as[8]

$$\mathcal{J}_c = \frac{1}{\bar{d}}\sigma_0 X_0 \tag{1}$$

Here, $\sigma_0$ is the yield stress, $X_0$ is the mean spacing between voids and $\bar{d}$ is a numerical factor in the range 0.5 to 1, depending upon the strain-hardening exponent and the degree of elastic mismatch between layer and substrate.

Fracture mechanism 2 is interfacial debonding near the tip, as shown in Fig. 1(b). It occurs when the near-tip stress normal to the interface $\sigma_{22}$ exceeds the bond strength of the weak interface. O'Dowd *et al.*[6] argue that the toughness can be estimated by assuming that the crack advances when $\sigma_{22}$ attains a critical value at a characteristic distance ahead of the crack tip. Shih and his colleagues[2,9] have shown that, under conditions of small-scale yielding or constrained large-scale yielding, the mode I opening-dominated state can be adequately represented by the HRR field as

$$\sigma_{ij} = \sigma_0 \left(\frac{\mathcal{J}}{\alpha\sigma_0\varepsilon_0 r}\right)^{1/n+1} h_{ij}(r, \theta) \tag{2}$$

where $\alpha$, $\varepsilon_0$ and $n$ are the material properties defined by the Ramberg–Osgood constitutive equation and $(r, \theta)$ are the distance from the crack tip and the angle from the interfacial plane, respectively. The function $h_{ij}$ is weakly dependent upon the radius $r$. If it is assumed that the fracture mechanism 2 operates when the tensile traction across the interface $\sigma_{22}$ reaches the critical value $C_A\sigma_0$ at a characteristic distance $r_c$, the toughness $\mathcal{J}_{c2}$ is derived from Eq. (2) as follows:

$$\mathcal{J}_{c2} = \alpha\sigma_0\varepsilon_0 r_c \left(\frac{C_A}{h_{22}(r_c, \theta)}\right)^{n+1} \tag{3}$$

Here, $C_A$ is the ratio of the cohesive strength of the interface to the yield strength of the layer.

Fracture mechanism 3 is high triaxiality cavitation at a distance of several $h$ ahead of the crack tip, as shown in Fig. 1(c), followed by void coalescence. The remote triaxiality develops when the interfacial bond is sufficiently strong to allow the ductile layer to undergo

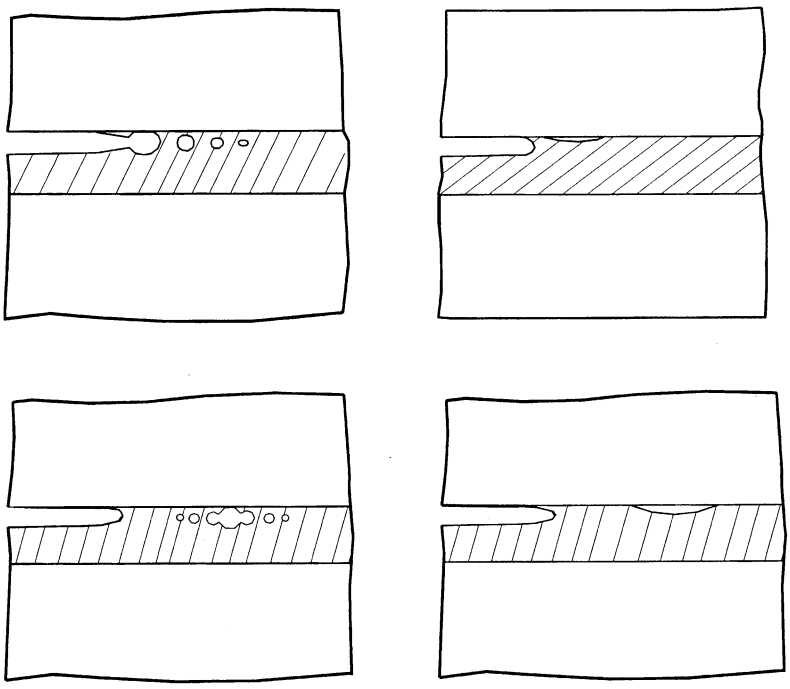

**Fig. 1** Four kinds of fracture mode in a sandwiched ductile layer. (a) Near-tip void growth and coalescence; (b) interface debonding near the crack tip; (c) high triaxiality cavitation ahead of the crack tip; (d) interface debonding ahead of the crack tip.

substantial plastic deformation. According to the cavitation criterion of Huang *et al.*,[10] a void grows unstably when the mean stress reaches a critical value $C_N\sigma_0$, where the coefficient $C_N$ is of the order of 4–6. Varias *et al.*[8] show that the toughness $\mathcal{J}_{c3}$ follows as

$$\mathcal{J}_{c3} = \left[ C_s^2 \cdot C_N^2 \cdot \frac{(1-\nu_s^2)}{E_s} \right] \sigma_0^2 h \tag{4}$$

where $E_s$ and $\nu_s$ are Young's modulus and Poisson's ratio of the stiff substrates, respectively. $C_s$ is a dimensionless proportionality constant defined as

$$C_s = \frac{1}{\sigma_m^*} \sqrt{\frac{\mathcal{J} E_s}{h(1-\nu_s^2)}}$$

which relates the maximum mean stress $\sigma_m^*$ developed in the ductile layer to the value of $\mathcal{J}$. Notet that $\mathcal{J}_{c3}$ is based on cavitation remote from the crack tip, and so the crack does not advance from its tip.

Fracture mechanism 4 is interface debonding at a distance of several $h$ ahead of the crack tip, as shown in Fig. 1(d). For the same reasons as discussed for fracture mechanism 3, the maximum value of the tensile traction across the interface $\sigma_{22}$ may occur far ahead of the tip. If the maximum value of $\sigma_{22}$ reaches the critical value $C_A\sigma_0$, then fracture mechanism 4 is assumed to be operative. The toughness is given by Varias *et al.*[8] as

$$\mathcal{J}_{c4} = \left[ C_x^2 \cdot C_A^2 \cdot \frac{(1-\nu_s^2)}{E_s} \right] \sigma_0^2 h \tag{5}$$

where $C_x$ (= 2–3) is a dimensionless proportionality constant defined as

$$C_x = \frac{1}{\sigma_{22}^*} \sqrt{\frac{\mathcal{J} E_s}{h(1-\nu_s^2)}}$$

which relates the maximum value of the stress $\sigma_{22}^*$ to the intensity of the $\mathcal{J}$-field. Tvergaard and Hutchinson[11] have made a similar estimate of the toughness as

$$\mathcal{J}_{c4} = \left[ \sqrt{3}\pi \cdot C_A^2 \cdot (C_A - 3) \frac{(1-\nu_s^2)}{E_s} \right] \sigma_0^2 h \tag{6}$$

and showed that Eq. (6) was valid for $C_A \geq 5$. We note the close proximity between Eqs (5) and (6).

When the stress intensity scaled by $K$ or $\mathcal{J}$ is so low that the plastic zone size does not span the layer thickness, $\sigma_{22}$ and $\sigma_m$ attain their maximum values near the crack tip. Therefore, if the mean spacing $X_0$ between voids is much less than the layer thickness $h$ ($X_0/h < 0.1$ according to Varias *et al.*[8]), or if the interface bond is weak, fracture mechanisms 1 and 2 are operative. Otherwise, fracture mechanisms 3 or 4 are triggered.

## EXPERIMENTS AND RESULTS

### Preparation of specimens

Specimens of CT/S (Compact Tension/Shear) geometry were manufactured, as sketched in Fig. 2. They consisted of a solder layer sandwiched between two thick brass blocks. This geometry was first used by Richard and Benitz[12] to measure the mixed-mode fracture toughness of homogeneous materials. Specimens were manufactured with two values of overall thickness, $t = 5$ mm and 10 mm and with two values of layer height, $h = 0.5$ mm and 2.0 mm. Thus, the $h/t$ equals 0.05, 0.1, 0.2, and 0.4. The chemical compositions and mechanical properties of the brass and solder are shown in Table 1. It is noted that Young's modulus and yield strength of the brass are about six times and nine times those of the solder, respectively.

The specimens were prepared as follows. First, the machined brass blocks were polished in the cracking direction or in the through-thickness direction using 400 μm grit emery paper. In order to obtain a strong bond between the brass and the solder, the brass surfaces were coated with an inorganic flux (Baker's soldering fluid No. 3) prior to casting of the solder between the brass blocks. A pre-crack along the upper interface of the solder and brass block was produced by vapour-depositing a 0.2 μm layer of aluminum on to one-half of bonding surface of one of the brass blocks, prior to application of the flux. Poor adhesion between this

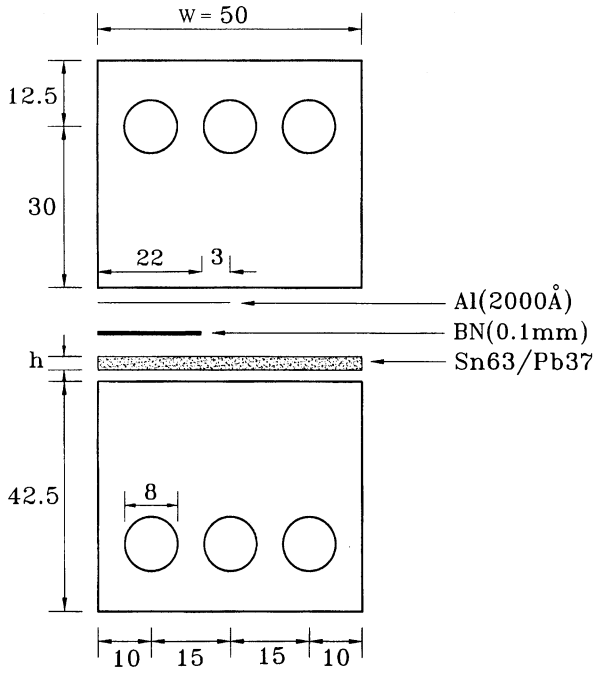


**Fig. 2** Configuration of the CT/S specimen.

**Table 1** Chemical compositions and mechanical properties of brass and solder

| | Chemical composition | Young's modulus, $E$ (GPa) | Poisson's ratio, $\nu$ | Yield stress, $\sigma_0$ (MPa) | Strain hardening exponent, $n$ | Strain hardening coefficient, $\alpha$ |
|---|---|---|---|---|---|---|
| Brass | 60Cu, 40Zn | 90 | 0.35 | 300 | – | – |
| Solder | 63Sn, 37Pb | 15 | 0.397 | $35 \pm 1$ | 10.7 | 0.85 |

aluminum layer and the solder was assured by the following two treatments after vapour deposition:

1 The aluminum was oxidized at 400°C for 1 h in an electric furnace.
2 Boron-nitride (BN) die release agent was applied to the oxidized aluminum. As the BN layer was 0.1 mm thick, there was concern that it would lead to a blunted pre-crack. To ensure that a sharp pre-crack was produced, the BN layer was terminated 3 mm from the end of the aluminum layer, as shown in Fig. 2.

After one of the brass blocks had been given the above pre-treatment, the rest of the bonding surface of both brass blocks were painted with Baker's fluid, and dried at 140°C for 30 min in an electric oven. The two brass blocks were then placed parallel to each other in a vacuum furnace, with the flux-painted surfaces facing each other. The gap between the blocks defined the final solder layer thickness $h$. Solder pieces were placed on top of the brass blocks and the materials were held at 220°C for 4–5 h so that the solder pieces melted into the gap between the brass blocks. Voids within the solder were extracted by repeated vacuum degassing. Finally, the cast brass/solder combination was machined to the CT/S specimen geometry.

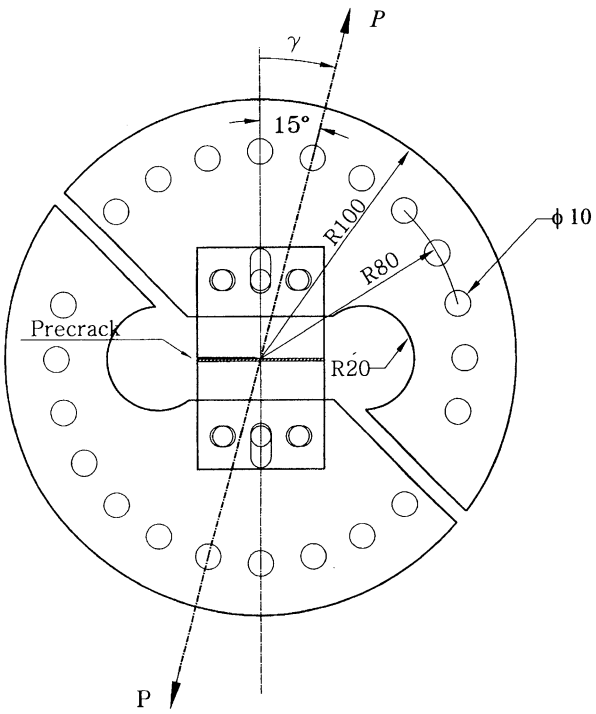


**Fig. 3** Grip and specimen assembly. Thickness of plate: 10 mm.

## Experimental procedure

Figure 3 shows the specimen and mixed-mode grip assembly; the arrangement is similar to that used by Richard and Benitz.[12] The loading angle $\gamma$ was varied over the range $\gamma = -45°$ to 15° with an interval of 15°. In order to ensure that a sharp pre-crack was formed, with no bridging of isolated solder ligaments across the pre-crack, fatigue pre-loading was applied using a maximum load per unit thickness of 140 N mm$^{-1}$, a load ratio of $R = 0.1$ and a loading angle of $\gamma = -15°$. (The maximum load of the fatigue cycle was determined by two-dimensional elastic–plastic finite element analysis so that the plastic zone size near the crack tip at the load did not exceed 20% of the solder layer thickness $h$.[13]) The side face of the specimen was monitored by a travelling microscope during the fatigue cycling and the fatigue loading was maintained until it was certain that no bridging across the pre-crack existed.

The pre-cracked specimens were fractured in a screw-driven test machine at a constant displacement rate of 0.1 mm min$^{-1}$, using five loading angles, $\gamma = -45°$, $-30°$, $-15°$, 0° and 15° for each of the four thickness ratios $h/t$. For each combination of $\gamma$ and $h/t$, three to six specimens were tested. The fracture events were monitored by a video camera and recorder.

## Loading angle and mode mix

In the linear elastic case, the mode mix at the interfacial crack tip can be related to the phase angle of loading, $\gamma$. The mode mix for a homogeneous specimen without a sandwich layer is defined by

$$\phi = \tan^{-1} \frac{K_{II}}{K_I} \tag{7}$$

where $K_I$ and $K_{II}$ are the mode I and II stress intensity factors, respectively. The mode mix for a crack along an interface between dissimilar elastic materials is defined

by[1]

$$\psi = \tan^{-1}\left(\frac{\sigma_{12}}{\sigma_{22}}\right)_{l=h} = \tan^{-1}\left[\frac{\mathrm{Im}(\boldsymbol{K}l^{i\varepsilon})}{\mathrm{Re}(\boldsymbol{K}l^{i\varepsilon})}\right]_{l=h} \quad (8)$$

where $\sigma_{12}$, $\sigma_{22}$ are the shear and normal stresses at a distance $l = h$ directly ahead of the crack tip, respectively. Here, $\boldsymbol{K}$ is the complex interfacial stress intensity factor, and $\varepsilon$ is a material mismatch parameter, related to the Dundur's parameter $\beta$ by

$$\varepsilon = \frac{1}{2\pi}\ln\left(\frac{1-\beta}{1+\beta}\right).$$

In turn, the Dundur's parameter $\beta$ is defined by

$$\beta = \frac{\mu_1(\kappa_2 - 1) - \mu_2(\kappa_1 - 1)}{\mu_1(\kappa_2 + 1) + \mu_2(\kappa_1 + 1)} \quad (9)$$

Here, the subscripts 1 and 2 refer to the substrate and the sandwiched layer for the upper interface, $\kappa \equiv 3 - 4\nu$ in the plane strain, $\nu$ is Poisson's ratio and $\mu$ is the shear modulus. The relation among the external loading angle $\gamma$ and the mode mixes $\phi$ and $\psi$ has been determined by elastic finite element calculations by Hong,[14] and his results are plotted in Fig. 4. It is clear that the phase angle $\psi$ is independent of the ratio of layer thickness $h$ to specimen width $w$ for the specimens used in this work ($h/w = 0.01$ and 0.04) at least. Further, the difference between $\phi$ and $\psi$ is nearly constant at 10° at any given value of $\gamma$, in agreement with the analysis of Suo and Hutchinson.[15] It is obvious that substantial plastic deformation occurs due to the high ductility of the intermediate layer and that the LEFM parameter $\psi$ does not work near the interfacial crack tip at least, although the homogeneous elastic $K$-field still works in region remote from the crack tip ($r \sim 10h$).[8] Therefore, in this paper we use $\phi$ as the parameter representing the mode mix.

## Observed mechanisms of crack advance

In all specimens tested, crack initiation began from the tip of the pre-existing crack. However, the subsequent crack growth depended upon the values of $h$, $t$ and the loading angle $\gamma$. (Refer to Kang *et al.*[16] for the details of the fracture process and final configuration.)

Some examples of the load–displacement ($P$–$\delta$) curves, with sketches of the associated fracture paths, are given in Figs 5 to 7. Figure 5 shows the results for a specimen of $h = 0.5$ mm, $t = 10$ mm and $\phi = -26°$: at peak load unstable interfacial crack growth occurred directly ahead of the pre-crack.

In contrast, for a specimen of $h = 2$ mm, $t = 10$ mm, $\phi = 7°$ [Fig. 6(a)], an interfacial crack advanced unstably ahead of the pre-crack for some distance, then another crack initiated and advanced along the opposite interface.

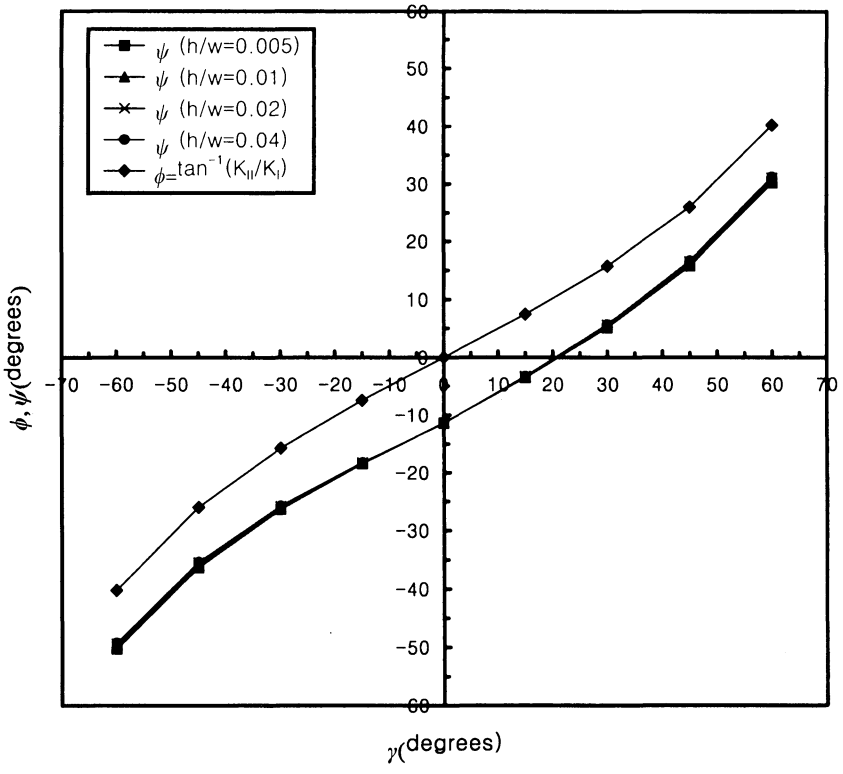


**Fig. 4** The phase angles $\phi$ and $\psi$, as a function of the external loading angle $\gamma$.[14] —■—, $\psi$ ($h/w = 0.005$); —▲—, $\psi$ ($h/w = 0.01$); —×—, $\psi$ ($h/w = 0.02$); —●—, $\psi$ ($h/w = 0.04$); —◆—, $\phi = \tan^{-1}(K_{II}/K_I)$.

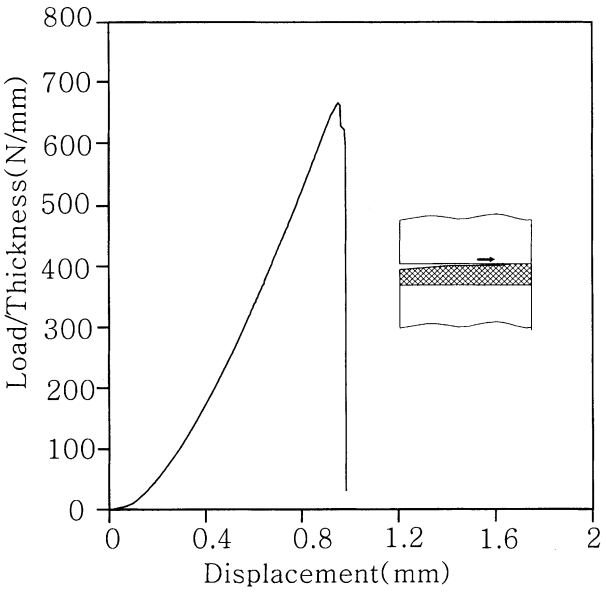


**Fig. 5** Load–displacement curve of the specimen, with $h =$ 0.5 mm, $t = 10$ mm and $\phi = 26°$ ($\gamma = -45°$), showing continued interfacial crack growth.

More than half of the specimens fractured by this mode of alternative debonding. Micrographs showing this mode are given in Figs 6(b) and (c). After interfacial crack advance by an increment of $l_c \approx (2 \sim 5)h$ along one interface, the crack jumped over to the opposite interface, in an alternating fashion.

The fracture response for the specimen of $h = 2$ mm, $t = 5$ mm, $\phi = -16°$ is given in Fig. 7; it fractured by overall plastic collapse of the ductile layer after some crack propagation along both interfaces.

The micro-mechanism of interfacial crack growth is by two mechanisms: (i) brittle debonding corresponding to the flat, silvery region (*) of the fracture surface shown in Fig. 6(c) and (ii) microvoid coalescence, corresponding to the grey, rough patches (**) on the fracture surface of Fig. 6(c). A scanning electron microscope (SEM) image of the brittle debonding mode is given in Fig. 8(a), whereas microvoid coalescence is shown in Fig. 8(b) for the case $h = 2$ mm; the dimple size increases from about 10 μm for the specimens with $h = 0.5$ mm to about 2.0 μm for $h = 2$ mm [Fig. 8(b)]. Figure 8(c) is an SEM micrograph of a region near the interface where two kinds of particles exist. One type is a $Cu_6Sn_5$ grain of size about 10 μm protruding into the solder. The other is a $\beta$-Sn precipitate mixed with intermetallics near the interface; the size is of the order of 2 μm. Microvoid coalescence occurred along the solder layer just beneath the brass/solder intermetallics $Cu_6Sn_5$, and brittle debonding occurred within the brass/solder intermetallics.[17]

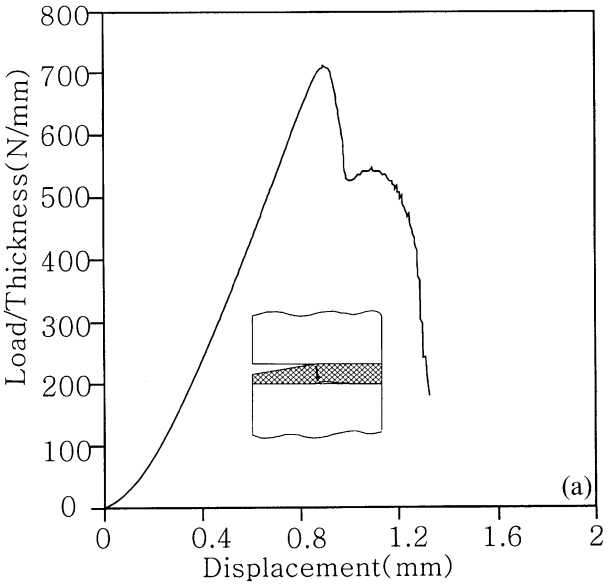


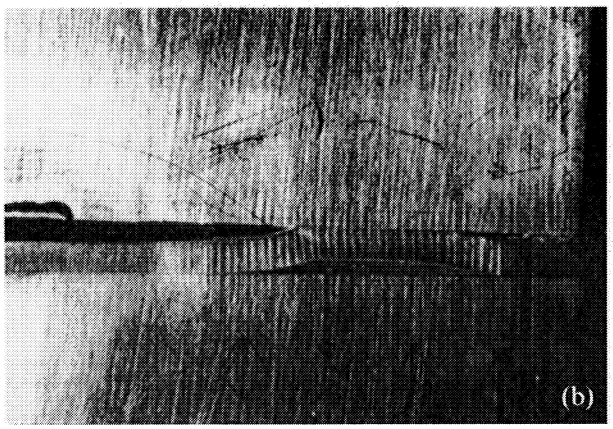


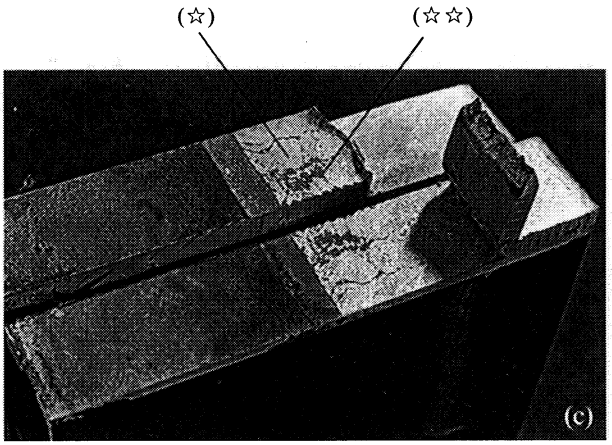


**Fig. 6** (a) Load–displacement curve of the specimen, with $h =$ 2 mm, $t = 10$ mm and $\phi = 7°$ ($\gamma = 15°$), showing the alternating mode of crack growth. (b) Side view: the dimension scale can be deduced from the layer thickness $h = 2$ mm. (c) Fracture surface showing that crack growth is along both interfaces. (*) denotes the region of brittle debonding and (**) denotes the region of microvoid coalescence.

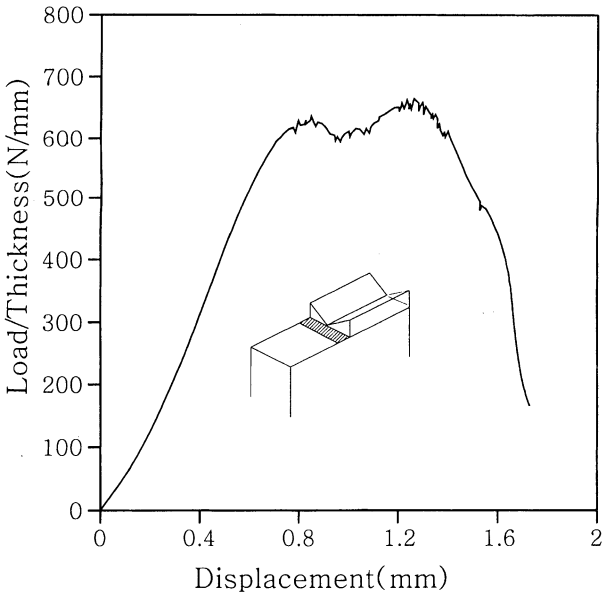


**Fig. 7** Load–displacement curve of the specimen, with $h = 2$ mm, $t = 5$ mm and $\phi = -16°$ ($\gamma = -30°$), showing plastic collapse by shear lip formation.

### Fracture toughness

The initiation toughness $\mathcal{J}_c$ was calculated from the initiation load $P_{cr}$ measured at the onset of crack propagation from the video recordings and $P$–$\delta$ curves. A finite element calibration of $\mathcal{J}$ as a function of load $P$ has already been performed by Hong[14] for the same material, geometry and loading as considered in this study.

The effect of phase angle $\phi$ upon $\mathcal{J}_c$ is shown in Figs 9(a) to (d). In the figures the symbol ◆ denotes a crack that propagates only along the upper interface for a distance of $h$ at least. The symbol ■ denotes a new crack that is initiated and propagates along the lower interface (i.e., alternative debonding) and the triangle denotes a crack that is initiated or propagates simultaneously along both interfaces at least in the initial phase of growth. The symbol ○ in Fig. 9(d) denotes that shear lips occur due to intensive plastic deformation through the layer thickness. For $h = 0.5$ mm and $t = 10$ mm (h/$t = 0.05$), as shown in Fig. 9(a), with the mode mixity $\phi < 0°$, most cracks propagate only along the upper interface, but with $\phi \geqslant 0°$, the trend towards the alternative debonding mechanism increases. On the contrary, for $h = 0.5$ mm and $t = 5$ mm ($h/t = 0.1$, that is, the lateral thickness $t$ is halved while $h$ is the same), as shown in Fig. 9(b), the alternative debonding mechanism occurs often even with $\phi < 0°$. However, despite the different crack propagation behaviour, the variation of toughness with mode mixity is similar. For $h = 2$ mm and $t = 5$ mm ($h/t = 0.4$), as shown in Fig. 9(d), in the range of mode mixity of $-16° \leqslant \phi \leqslant 0°$ intensive shear lips due to overall plastic collapse, as shown in the sketch of Fig. 7, occur on the fracture surface. This will be discussed later.

For $h = 0.5$ mm, $\mathcal{J}_c$ is in the range 300–900 J m$^{-2}$, with a maximum at around $\phi = -10°$. On the other hand, for $h = 2$ mm, $\mathcal{J}_c$ is somewhat higher in the range 500–1400 J m$^{-2}$. A consistent trend emerges between the mode mix and the magnitude of the toughness. For all values of $h$ and $t$ considered, $\mathcal{J}_c$ has a maximum at $\phi \approx -10°$; this trend is quite different from previous observations for brittle interfacial fracture[1] where the toughness is a minimum at a phase angle close to zero, and increases sharply with increasing mode II component.

## DISCUSSION

### Estimation of the mode I toughness for each fracture mode

The toughness under mode I loading is now estimated for each of the fracture modes 1 to 4, as summarized in Fig. 1. Consider first fracture initiation by microvoid coalescence at the crack tip. If the average dimple sizes found on the fracture surface (10 μm for $h = 0.5$ mm, 20 μm for $h = 2$ mm) are chosen as the values for the void spacing $X_0$, and if $1/\bar{d} = 1.25$ referring to Varias *et al.*,[8] Eq (1) gives

$$\mathcal{J}_{c1} = 438 \text{ J m}^{-2} \quad \text{for } h = 0.5 \text{ mm} \quad \text{and}$$

$$\mathcal{J}_{c1} = 875 \text{ J m}^{-2} \quad \text{for } h = 2 \text{ mm}$$

Now take the characteristic distance $r_c$ as the average grain size of the intermetallics (20 μm), and take $C_A = 3 \sim 10$ from Varias *et al.*;[8] then, the predicted interfacial toughness $\mathcal{J}_{c2}$ for crack advance from the crack tip follows from Eq. (3) as

$$\mathcal{J}_{c2} = 760 \sim 1 \times 10^9 \text{ J m}^{-2}$$

Note that $\mathcal{J}_{c2}$ is independent of the layer thickness $h$ and the upper limit is unreasonable. This will be discussed below. Next, consider cavitation ahead of the initial crack tip, mechanism 3. On taking $C_N = 5$ and $C_s = 3.1$ from Huang *et al.*[10] and Varias *et al.*,[8] respectively, Eq. (4) gives

$$\mathcal{J}_{c3} = 1435 \text{ J m}^{-2} \quad \text{for } h = 0.5 \text{ mm} \quad \text{and}$$

$$\mathcal{J}_{c3} = 5739 \text{ J m}^{-2} \quad \text{for } h = 2 \text{ mm}$$

Decohesion ahead of the crack tip, mechanism 4 is estimated by Eq. (5), upon taking $C_x = 2.8$ and $C_A = 3 \sim 10$ from Varias *et al.*,[8] to give

$$\mathcal{J}_{c4} = 421 \sim 4682 \text{ J m}^{-2} \quad \text{for } h = 0.5 \text{ mm} \quad \text{and}$$

$$\mathcal{J}_{c4} = 1684 \sim 18\,728 \text{ J m}^{-2} \quad \text{for } h = 2 \text{ mm}$$

Unrealistically high values of toughness are obtained by

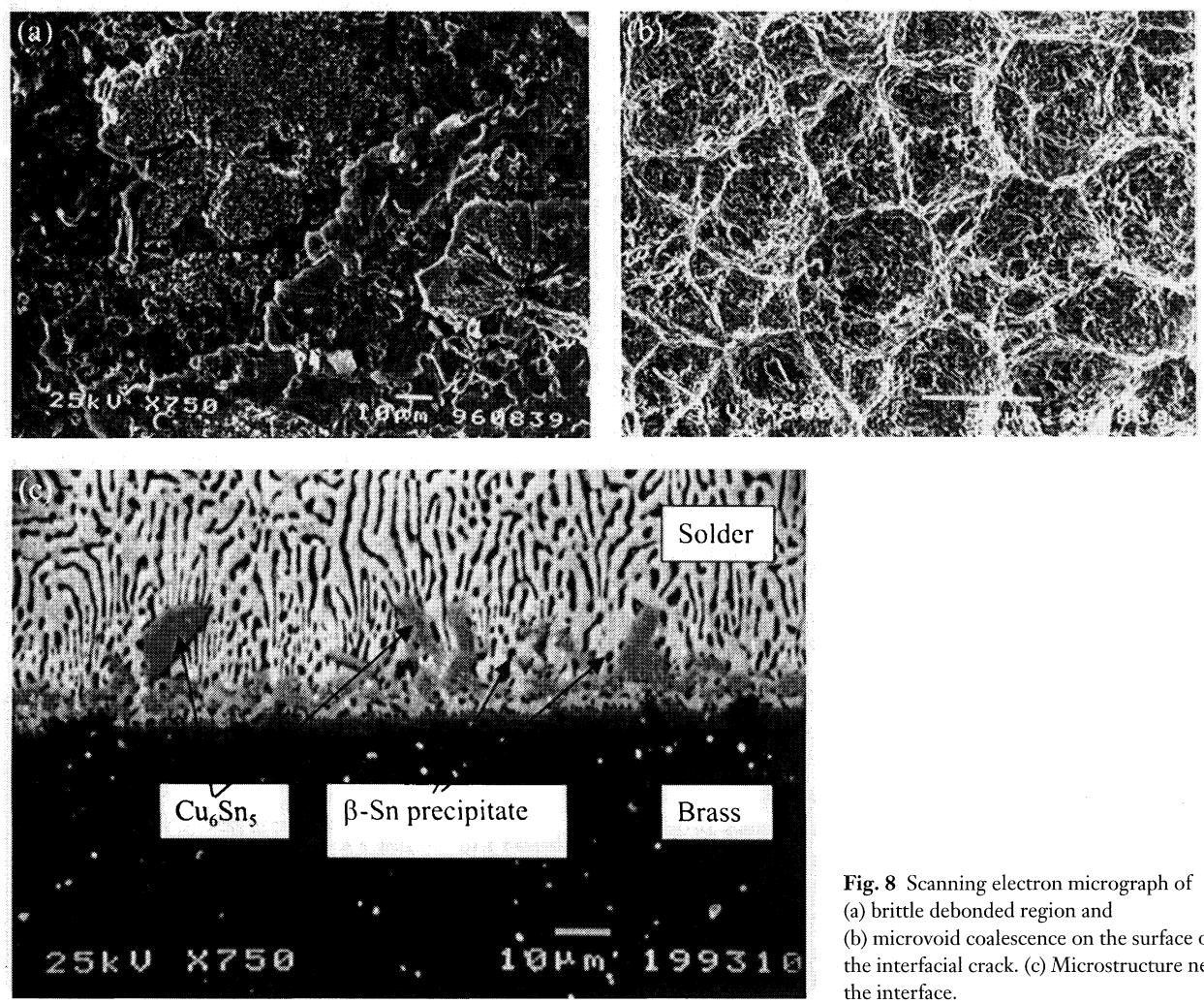


**Fig. 8** Scanning electron micrograph of (a) brittle debonded region and (b) microvoid coalescence on the surface of the interfacial crack. (c) Microstructure near the interface.

the alternative relation, Eq. (6), valid for $C_A \geqslant 5$: for $C_A = 5 \sim 10$, Eq. (6) gives

$$\mathcal{J}_{c4} = 3217 \sim 28\,372 \text{ J m}^{-2} \quad \text{for } h = 0.5 \text{ mm} \quad \text{and}$$
$$\mathcal{J}_{c4} = 12\,870 \sim 113\,490 \text{ J m}^{-2} \quad \text{for } h = 2 \text{ mm}$$

We suppose that the estimates given by Eq. (5) are realistic.

The value of the ratio $C_A$, which scales the bond strength of the interface to the layer yield strength, has a large influence on the accuracy of the predictions by Eqs (3), (5) and (6). Ideally, the value of $C_A$ should be evaluated from an indepedent measurement of the strength of the intermetallics, $Cu_6Sn_5$; this proved difficult to achieve, experimentally, because it is hard to make a tensile specimen of homogeneous $Cu_6Sn_5$. In particular, the accuracy of the prediction, Eq. (3), is very sensitive to the assumed value of $C_A$ due to the presence of the $C_A^{n+1}$ term, and this leads to a substantial uncertainty in the predicted value of $\mathcal{J}_{c2}$. It is thought that this intrinsic variability of toughness results in a variation of the actual fracture process within the same specimen.

The measured mode I toughness $\mathcal{J}_c$ at $\phi = 0$ is $650 \pm 100 \text{ J m}^{-2}$ for $h = 0.5$ mm, as shown in Fig. 9(a); these values are similar to the predictions $\mathcal{J}_{c1}$, $\mathcal{J}_{c2}$ or $\mathcal{J}_{c4}$ corresponding to the fracture mechanisms 1, 2 or 4, respectively. When $h = 2$ mm, and $\phi = 0$, the measured $\mathcal{J}_c$ equals $1000 \pm 100 \text{ J m}^{-2}$ in agreement with the predictions $\mathcal{J}_{c1}$ or $\mathcal{J}_{c2}$, corresponding to the fracture mechanisms 1 or 2. Both mechanisms result in crack growth from the pre-crack tip. According to the finite element analysis by Kim,[18] the mechanisms 3 and 4 are operative when $\mathcal{J}/\sigma_0 h \geqslant 0.04$, that is, $\mathcal{J} \geqslant 700 \text{ J m}^{-2}$ for $h = 0.5$ mm and $\mathcal{J} \geqslant 2800 \text{ J m}^{-2}$ for $h = 2$ mm. In comparison with the experimental results, the mechanism 4 may be operative for thinner layers ($h = 0.5$ mm), but not for thicker ones ($h = 2$ mm). That agrees with the estimation of the fracture mechanism mentioned above.

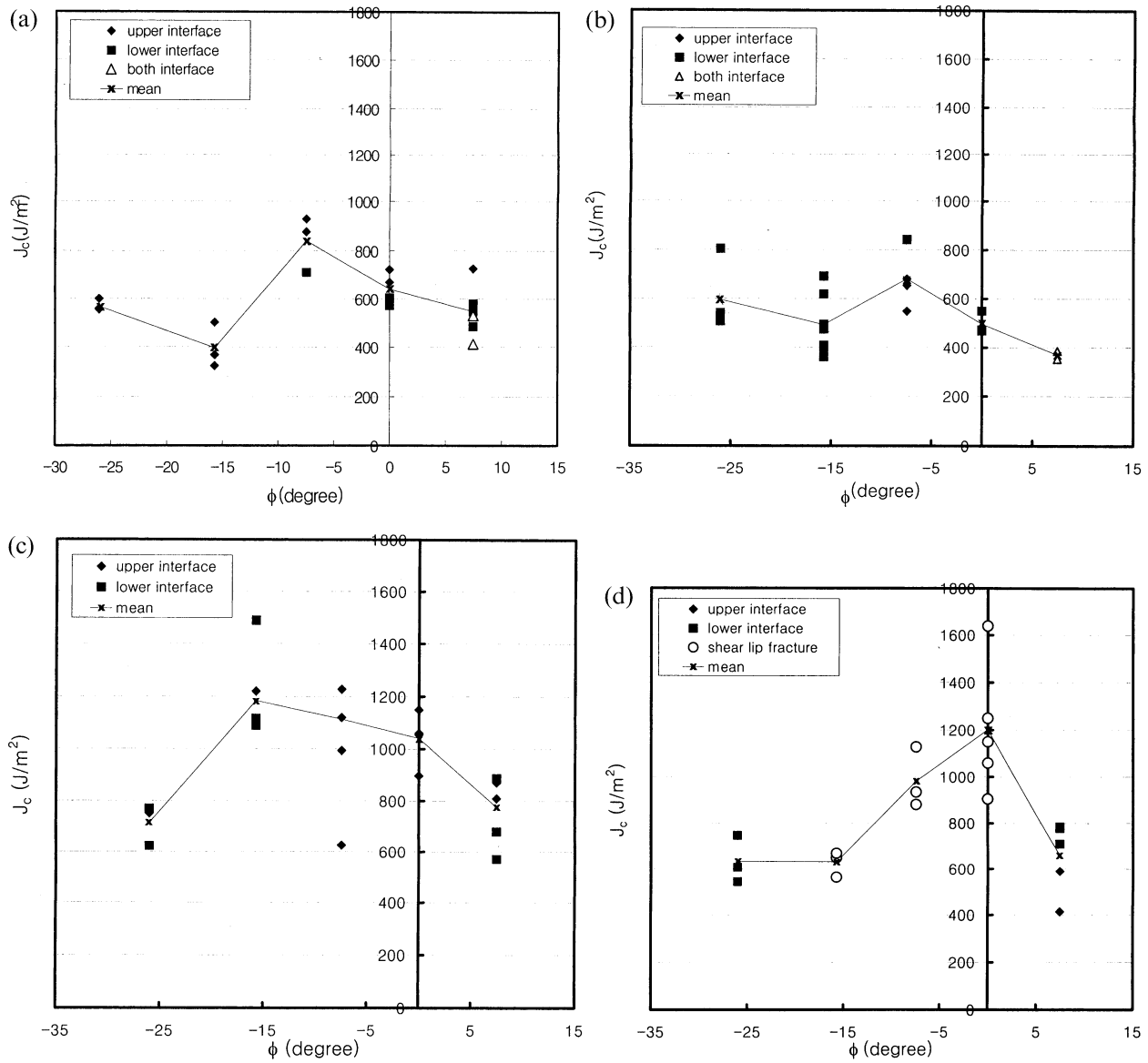


**Fig. 9** Measured initiation toughness $\mathcal{J}_c$ versus phase angles $\phi$ for (a) $h = 0.5$ mm, $t = 10$ mm; (b) $h = 0.5$ mm, $t = 5$ mm; (c) $h = 2$ mm, $t = 10$ mm; and (d) $h = 2$ mm, $t = 5$ mm. ◆, upper interface; ■, lower interface; △, both interfaces; —×—, mean; ○, shear lip fracture.

In fact, near-tip crack growth (fracture mechanisms 1, 2) could not be clearly distinguished from remote crack initiation (fracture mechanisms 3, 4) during the fracture experiments, and on the fracture surfaces the dimpled area and flat area are often mixed up, as shown in Fig. 6(c). The proportion of the dimpled and flat areas gives information only about competition between microvoid coalescence (fracture mechanisms, 1, 3) and brittle debonding (fracture mechanisms 2, 4). Figures 10(a) and (b) show the variations of the ratio of the dimpled area $A_d$ to total area $A$ of the fracture surface up to the distance $r = 1h$ and $r = 2h$ ahead of the initial crack-tip with the mode mixities. The scatter among specimens is often very large. It may come from the quality of specimen preparation, but also it may be regarded as the consequence of severe competition among the fracture mechanisms. When $h = 0.5$ mm, $t = 10$ mm and $\phi = 0°$, the ratio $A_d/A$ is highly variable within the range from $A_d/A = 0.0$ to 1.0 as shown in Fig. 10(a). In this case the estimations $\mathcal{J}_{c1}$, $\mathcal{J}_{c2}$ and $\mathcal{J}_{c4}$ are comparable with each other, as mentioned above. That mean that the real fracture mechanism is uncertain, which yields the large scatter of $A_d/A$. On the contrary, when $h = 2$ mm, $t = 10$ mm and $\phi = 0°$, the ratio $A_d/A = 0.25 \pm 0.15$, as shown in Fig. 10(b), which means that brittle debonding due to the mechanism 2 is governing.

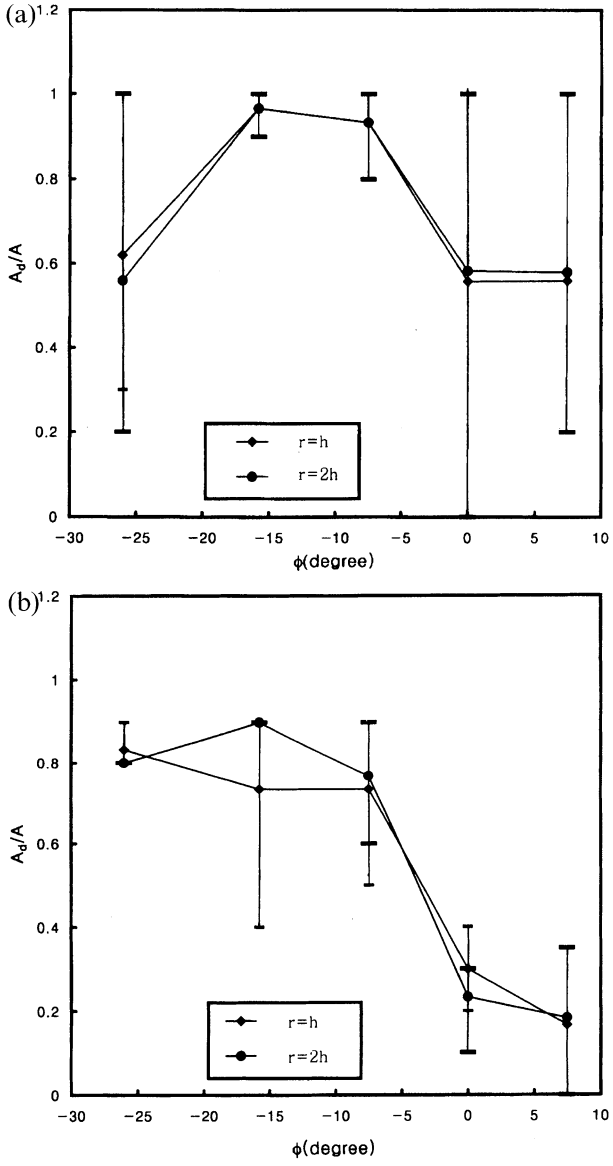


**Fig. 10** The ratio of dimpled area to total area up to distance $h$ and $2h$ ahead of the initial crack tip; (a) $h = 0.5$ mm, $t = 10$ mm; (b) $h = 2$ mm, $t = 10$ mm. ◆, $r = h$; ●, $r = 2h$.

## Effect of mode mix upon fracture mode

Previous experimental investigations for brittle interfacial fracture have shown that the toughness has the lowest value for pure mode I and increases with increasing mode II component, regardless of its sign. Evans and Hutchinson[19] have explained this in terms of 'crack-tip shielding' associated with fracture surface roughness. O'Dowd *et al.*[6] have argued that the toughness variation with mode mix can be predicted using the maximum loop stress criterion for the case of near-tip debonding, that is, for fracture mechanism 2. Similar toughness variations have been predicted for fracture mechanisms 3 and 4 by Varias *et al.*[20] and for mechanism 4 by Tvergaard and Hutchinson.[11] They explained that the mode II component of loading reduced the stress triaxiality in the sandwich layer and increased the toughness.

Thurston and Zehnder[7] have observed an asymmetric dependence of toughness upon mode mix, for silica/copper/silica sandwich specimens. (In their specimens the initial crack was on the lower interface of the ductile copper layer, hence the sign of the mode mix is opposite to that of the current study.) For positive values of mode mix the toughness increased with phase angle, whereas for a negative mode mix the toughness decreased with increasing mode II component. The asymmetric toughness variance with regard to the mode mix has also been reported by Liechi and Chai,[21] but it their case the asymmetry is easily compensated by some shift of the mode mix.

Kim[18] has recently explored the dependence of the crack tip opening upon the sign of phase angle for an interface crack of the same material combination as in this work. As an example, Fig. 11 displays the crack tip profile corresponding to $\phi = +30°$ and $-30°$, respectively. Crack advance from the tip by microvoid coalescence (mechanism 1) and by decohesion (mechanism 2) are substantially influenced by local crack tip profile. Aoki *et al.*[22,23] and, more recently, Gosal and Narasimhan[24,25] have performed finite element analysis to demonstrate such a dependence of the fracture toughness upon mode-mix; they considered microvoid coalescence within a homogeneous ductile material. Consequently, the asymmetry of the measured toughness with phase angle might be explained in terms of the near-tip state for an interfacial crack. On the other hand, the fracture mechanisms 3 and 4 are expected to be almost independent of the sign of mode mix because both of them occur at several layer thicknesses ahead of the tip, whereas the stress and deformation are controlled

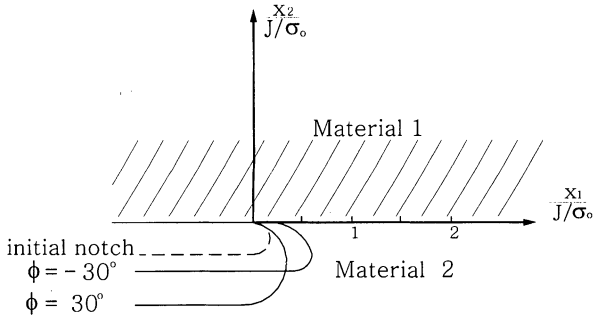


**Fig. 11** Crack tip profile, corresponding to $\phi = -30°$, 0° and 30°, for $\mathcal{J}^{\infty}/\sigma_0 h = 0.02$.[18]

not by the near-tip singularity but by the remote field as described in Varias *et al.*[8]

As shown in Figs 10(a) and (b), the proportion of the dimpled area on the fracture surface near the initial crack tip $A_d/A$ is quite changeable with the mode mixity. The large scatter often observed reflects the uncertainty of fracture mechanism as mentioned earlier. Roughly speaking, in cases of $\phi < 0$ the dimpled area is predominant, but in cases of $\phi \geq 0$ the proportion of the flat surface due to the likelihood of brittle debonding becomes larger. However, any clear relationship with the variance of the fracture toughness, $\mathcal{J}_c$ in Figs 9(a) to (d) was not found.

More than half of the specimens fractured by alternative debonding, as shown in Fig. 6(b), that is, after interfacial crack advance by an increment of $l_c \approx (2 \sim 5)h$ along one interface, the crack jumped over to the opposite interface, in an alternating fashion. As shown in Figs 9(a) to (d), the switch among crack growth patterns obviously depends upon the mode mixity and $h/t$. However, it cannot be explained by the mechanisms of Fig. 1; it needs a full field solution of the constrained layer. Also, the effect of shear deformation which occurs prominently along the upper and lower interfaces under mixed-mode load should be taken into account to estimate microvoid coalescence. An independent study, involving experiments with a wider mixity and finite element analysis[26] inter-relates the fracture toughness, dimpled area ratio, mode mixity and fracture mechanism.

### Effect of constraint by elastic substrates

The fracture mechanism is significantly affected by the constraint due to the elastic substrates. In particular, the mechanisms 3 and 4 are operative when the interfacial strength is sufficiently high to allow a peak stress to develop far ahead of the crack tip; the estimates by Eqs (4)–(6) of the toughness each suggest that the toughness is proportional to the layer thickness. The fracture mechanisms 1 and 2 are also influenced by the presence of the elastic substrates, due to crack tip shielding, as discussed by Varias *et al.*:[8] the crack tip $\mathcal{J}$-value is less than the remote value, due to non-proportional stressing associated with constrained plastic flow in the layer.

In ductile fracture of homogeneous materials, the intensity of hydrostatic stress, that is, the stress triaxiality which develops by constraint of plastic deformation near the crack tip is closely related to the near-tip void growth and coalescence which is a major mechanism of ductile fracture. Generally, voids in a material grow in proportion to the stress triaxiality. Hence, the higher constraint produces larger dimples on the fracture surface. (See Brownrigg *et al.*[27] and Sun[28]) On the contrary, if two different sizes of voids exist together, Tvergaard[29] has shown that under low stress triaxiality ($\sigma_m < 3\sigma_0$), only large voids grow steadily whereas small voids hardly grow, but under high stress triaxiality ($\sigma_m > 3\sigma_0$) the large voids keep growing steadily whereas the small voids grow rapidly so as to lead to unstable cavitation. The unstable growth of small voids has been analysed also by Faleskog and Shih.[30] They found that the small voids among the large voids grew quickly under the high stress triaxiality until they had almost the same size as the large voids.

In the specimens of this work two kinds of particles exist near the interface as shown in Fig. 8(c). One kind is $Cu_6Sn_5$ grains the size of which are of the order of 10 μm, and the other is β-Sn precipitates the size of which are of the order of 2 μm. Neither of them are so tightly coherent with the surrounding matrix that they might behave like voids under plastic deformation.[31] Therefore we may make an estimation about the interrelation between dimple size and $h$ as follows: if $h$ is small, the rigid substrates start to suppress the plastic deformation of the intermediary solder layer early and then high triaxiality ($\sigma_m > 3\sigma_0$) develops in front of the crack tip. Consequently, according to Faleskog and Shih,[30] voids grow rapidly from the small particles; that is, β-Sn precipitates until having a similar size to the large particles of $Cu_6Sn_5$, which leads to early void coalescence, namely, low fracture toughness. On the contrary, if $h$ is large, the constraint by the substrates is delayed until the plastic zone size grows enough in comparison with the layer thickness $h$, and the triaxiality remains low even with high external load. Consquently, the voids hardly grow from the β-Sn precipitates whereas the voids from the large $Cu_6Sn_5$ grains grow steadily, which leads to delay of void coalescence, namely, enhancement of fracture toughness. As shown in Fig. 9 under mode I load the measurements of $\mathcal{J}_c$ are 650 J m$^{-2}$ and the dimple size is 10 μm on average for $h = 0{\cdot}5$ mm, whereas these measurements are 1000 J m$^{-2}$ and 20 μm on average for $h = 2$ mm, respectively. These results demonstrate that our earlier estimation is reasonable.

For the specimen in this work, the uncracked ligament $(w) - (a)$ is much larger than the lateral specimen thickness $t$ or the layer thickness $h$, so overall deformation of the layer could tkae place in the $h$ or $t$ direction except near the crack tip, and deformation in the direction of the specimen width $w$ is negligible. When the thickness $t$ of the specimen is not large in comparison with the layer height $h$, plastic collapse can occur in the through-thickness direction, and the net section strength of the layer can be estimated from Hill's slip-line field[32] of plane strain compression. Dalgleish *et al.*[33] obtained the limit stress $\sigma_{limit}$ corresponding to the solution, as

follows:

$$\frac{\sigma_{\text{limit}}}{\sigma_0} = \frac{3}{4} + \frac{1}{4}\left(\frac{t}{h}\right) \tag{10}$$

This equation is applicable for a normal external load, that is, $\gamma = \phi = 0°$. Here, the effects of brittle debonding and ductile void growth are neglected, and so Eq. (10) can be used to predict the bond strength corresponding to plastic collapse within the ductile layer, and not due to crack growth. In fact, for $h/t = 0.4$ and $\phi = 0$, the measured maximum normal stress, i.e., the maximum load divided by $(w - a) \times t$, is $1.06\sigma_0 \sim 1.29\sigma_0$, which is close to the limit stress ($\sigma_{\text{limit}} = 1.38\sigma_0$) estimated by Eq. (10). Furthermore, the intensive shear lips were observed on the fracture surface as shown in the sketch of Fig. 7 (or see reference 16).

## CONCLUSIONS

A combined experimental and theoretical analysis of the fracture behaviour of brass/solder/brass sandwich has been conducted. The effects of mode mix and plastic constraint on the fracture behaviour of the interface crack have been explored, and the following conclusions have been obtained.

1 For mode I loading of two thicknesses of the solder layer ($h = 0.5$ mm and 2 mm), the crack initiates by near tip void growth or by ductile debonding. Brittle debonding also occurs at a distance of several layer thicknesses ahead of the crack, for the case of the thinner solder layer ($h = 0.5$ mm).
2 The dependence of toughness upon the mode-mix relation is different from that observed for elastic–brittle material systems. Here, the observed toughness decreases with increasing mode II component.
3 The toughness increases with increasing thickness of the ductile intermediary layer until plastic collapse of the layer intervenes, resulting in shear-lip formation.

### Acknowledgements

The authors are grateful to Dr Amal Esawi for giving valuable information at the initial stage of this work and also to Mr Ki-Ju Hong and Mr Dong-Hak Kim for providing results of their finite element analysis and stimulating discussion. K.J.K., S.H.C. and B.G.S. are supported by the Korea Science and Engineering Foundation through a grant on 'Fracture Mechanics Study on Reliability in Packages of Microelectronic Devices' (contact KOSEF 94-0200-02-02-3).

## REFERENCES

1 J. W. Hutchinson and Z. Suo (1991) Mixed mode cracking in layered materials. *Adv. Appl. Mech.* **29,** 63–191.
2 C. F. Shih and R. J. Asaro (1989) Elastic–plastic of cracks on bimaterial interfaces: part II—structure of small-scale yielding field. *J. Appl. Mech.* **56,** 763–779.
3 I. E. Reimanis, B. J. Dalgleish and A. G. Evans (1991) The fracture resistance of a model metal/ceramic interface. *Acta Metall. Mater.* **39,** 3133–3141.
4 A. G. Evans and B. J. Dalgleish (1993) The fracture resistance of metal–ceramic interfaces. *Mater. Sci. Engng* **A162,** 1–13.
5 H. C. Cao and A. G. Evans (1989) An experimental study of the fracture resistance of bimaterial interfaces. *Mech. Mater.* **7,** 295–304.
6 N. P. O'Dowd, M. G. Stout and C. F. Shih (1992) Fracture toughness of alumina–niobium interfaces; experiments and analyses. *Phil. Mag.* **66,** 1037–1064.
7 M. E. Thurston and A. T. Zehnder (1993) Experimental determination of silica/copper interfacial toughness. *Acta Metall. Mater.* **41,** 2985–2992.
8 A. G. Varias, Z. Suo and C. F. Shih (1991) Ductile failure of a constrained metal foil. *J. Mech. Phys. Solids* **39,** 963–986.
9 C. F. Shih, R. J. Asaro and N. P. O'Dowd (1991) Elastic–plastic analysis of cracks on bimaterial interfaces: part III large scale yielding. *J. Appl. Mech.* **58,** 450–463.
10 Y. Huang, J. W. Hutchinson and V. Tvergaard (1991) Cavitation instabilities in elastic–plastic solids. *J. Mech. Phys. Solids* **39,** 223–241.
11 V. Tvergaard and J. W. Hutchinson (1996) On the toughness of ductile adhesive joints. *J. Mech. Phys. Solids* **44,** 789–800.
12 H. A. Richard and K. A. Benitz (1983) A loading device for the criterion of mixed mode in fracture mechanics. *Int. J. Fract.* **22,** R55–58.
13 Y.-C. Park (1995) Experiments of brass/solder interfacial fracture. Masters Thesis. Chonnam National University, Korea.
14 K.-J. Hong (1995) Finite element analysis on elasto-plastic interfacial fracture of a bimaterial sandwich specimen. Masters Thesis. Chonnam National University, Korea.
15 Z. Suo and J. W. Hutchinson (1989) Sandwich test specimens for measuring interface crack toughness. *Mater. Sci. Engng* **A109,** 135–143.
16 K.-J. Kang, B.-G. Song and Y.-C. Park (1998) Fracture of a ductile layer constrained by stiff substrates—Part I: experimental observations. *KSME Trans. A* **22,** 2221–2230.
17 S.-H. Choi (1998) Strength analysis on the solder joint of the electronic package using fracture mechanics. Masters Thesis. Chonnam National University, Korea.
18 D.-H. Kim (1998) The fracture mechanical analysis of crack propagation behavior in a ductile layer sandwiched by elastic bodies. Masters Thesis. Chonnam National University, Korea.
19 A. G. Evans and J. W. Hutchinson (1989) Effect of non-planarity on the mixed mode fracture resistance on bimaterial interfaces. *Acta Metall. Mater.* **37,** 909–916.
20 A. G. Varias, Z. Suo and C. F. Shih (1992) Mode mix effect on the damage of a constrained ductile layer. *J. Mech. Phys. Solids* **40,** 485–509.
21 K. M. Liechti and Y. S. Chai (1992) Asymmetric shielding in interfacial fracture under in-plane shear. *J. Appl. Mech.* **59,** 295–304.
22 S. Aoki, K. Kishimoto, T. Yoshida, M. Sakata and H. A. Richard (1990) Elastic–plastic fracture behaviour of an aluminum alloy under mixed mode loading. *J. Mech. Phys. Solids* **38,** 195–213.
23 S. Aoki, K. Kishimoto, T. Yoshida and M. Sakata (1987) A finite element study of the near tip deformation of a ductile material under mixed mode loading. *J. Mech. Phys. Solids* **35,** 431–455.

24 A. K. Ghosal and R. Narasimhan (1996) Mixed mode fracture initiation in a ductile material with a dual population of second phase particles. *Mater. Sci. Engng* **A211,** 117–127.
25 A. K. Ghosal and R. Narasimhan (1996) Numerical simulations of hole growth and ductile fracture initiation under mixed mode loading. *Int. J. Fract.* **77,** 281–304.
26 K.-J. Kang, D.-H. Kim and S.-H. Choi (in press) Effect of mode mix upon fracture behaviors of a solder joint. *Int. J. Fract.*
27 A. Brownrigg, W. A. Spitzig, O. Richmond, D. Teirlinck and J. D. Embury (1983) The influence of hydrostatic pressure on the flow stress and ductility of a spheroidized 1045 steel. *Acta Metall. Mater.* **31,** 1141–1150.
28 J. Sun (1991) Effect of stress triaxiality on micro-mechanisms of void coalescence and micro-fracture ductility of materials. *Engng Fract. Mech.* **39,** 799–805.
29 V. Tvergaard (1990) Failure by ductile cavity growth at a metal/ceramic interface. Internal Report of the Danish Center for Applied and Mathematics and Mechanics, No. 406. The Technical University of Denmark, Lyngby, Denmark.
30 J. Faleskog and C. F. Shih (1997) Micromechanics of coalescence—I. Synergistic effects of elasticity, plastic yielding and multi-size-scale voids. *J. Mech. Phys. Solids* **45,** 21–50.
31 D. R. Frear, S. N. Burchett and H. S. Morgan (1994) *The Mechanics of Solder Alloy Interconnects.* Van Nostrand Reinhold, New York, NY, pp. 7–41.
32 R. Hill (1971) *Mathematical Theory of Plasticity.* Oxford University Press, Oxford, UK, pp. 226–230.
33 B. J. Dalgleish, M. C. Lu and A. G. Evans (1998) The strength of ceramics bonded with metals. *Acta Metall.* **36,** 2029–2035.